

# Robust trapping of 2D excitons in an engineered 1D potential from proximal ferroelectric domain walls.

P. Soubelet,<sup>1,\*</sup> Y. Tong,<sup>1</sup> A. Astaburuaga Hernandez,<sup>1</sup> P. Ji,<sup>1</sup> K. Gallo,<sup>2</sup> A. V. Stier,<sup>1</sup> and J. J. Finley<sup>1</sup>

<sup>1</sup>*Walter Schottky Institut and TUM School of Natural Sciences, Technische Universität München, Am Coulombwall 4, 85748 Garching, Germany.*

<sup>2</sup>*Department of Applied Physics, KTH Royal Institute of Technology, Roslagstullsbacken 21, Stockholm SE-106 91, Sweden.*

(Dated: 2025-03-21)

We investigate the confinement of neutral excitons in a one-dimensional (1D) potential, engineered by proximizing hBN-encapsulated monolayer MoSe<sub>2</sub> to ferroelectric domain walls (DW) in periodically poled LiNbO<sub>3</sub>. Our device exploits the nanometer scale in-plane electric field gradient at the DW to induce the dipolar exciton confinement via the Stark effect. Spatially resolved photoluminescence (PL) spectroscopy reveals the emergence of narrow emission lines redshifted from the MoSe<sub>2</sub> neutral exciton by up to  $\sim 100$  meV, depending on the sample structure. The spatial distribution, excitation energy response and polarization properties of the emission is consistent with signatures of 1D-confined excitons. The large electric field gradients accessible via proximal ferroelectric systems open up new avenues for the creation of robust quantum-confined excitons in atomically thin materials and their heterostructures.

The confinement of particles to length scales comparable to their de Broglie wavelength leads to the quantization of their motional ground states [1]. When the thermal energy of the system,  $E_T \simeq k_B T$ , falls below the energy separation between these confinement-induced states, its quantum nature emerges, altering properties such as the energy spectrum of fundamental excitations. Reliable quantum technologies hinge on the precise manipulation of particles in this quantum regime [2–5]. Furthermore, particle-particle interactions are significantly enhanced by reducing the dimensionality of a system [6–17], enabling the exploration of emergent quantum phases driven by the new interactions between these particles [18–24]. In this context, monolayer transition metal dichalcogenides (1L-TMDs) have emerged as a promising semiconductor platform due to their inherent two-dimensional (2D) confinement. These materials are direct band-gap at the  $K/K'$  points of their hexagonal Brillouin zone [25–27], where interband optical transitions form tightly bound excitons [28–32]. While excitons in 1L-TMDs couple strongly to light, achieving their motional quantization remains particularly challenging due to the heavy exciton masses and small exciton Bohr radius [31, 32]. For example, an energy splitting between discrete confined motional ground states of  $\hbar\omega \gtrsim 1$  meV, requires a confinement length scale of  $\ell_n = \sqrt{\frac{\hbar}{m_X \omega}} \lesssim 10$  nm for an exciton mass ( $m_X$ ) of the order of the free electron mass ( $m_e$ ) [33].

The manipulation of excitons in 2D-semiconductor materials has largely centered around approaches such as moiré potential engineering [8, 23, 34–36], nanopillars and strain engineering [3, 37–41], electron and ion beam irradiation [42, 43], and the local tuning of the dielectric environment [29, 44–49] to create interlayer junctions

and trapping potentials. The use of partially overlapping gates [33, 50, 51], has recently been shown to be a powerful approach to generate 1D exciton states [33, 50] and to enable control of exciton wave functions [51]. This method utilizes the DC Stark shift induced by an in-plane electric field [52], in combination with the formation of lateral  $p-i-n$  junctions where the  $p$ - and  $n$ -regions are defined by the gate arrangement [33, 50, 51, 53] to create a total exciton confinement potential. This technique offers the advantage of in-situ tuning of the confinement potential from a continuum of 2D exciton states to the 1D quantum regime, where excitons are confined within potential traps of the order of  $\sim 5$  meV. However, as the total confinement potential arises from the DC Stark shift and a sizeable repulsive Coulomb interaction [33], the motional ground states are susceptible to electronic noise and the composition of the 1D exciton wavefunction continuously varies with electron density and subband number [33].

In this work, we demonstrate how nanometer scale ferroelectric domain boundaries in lithium niobate (LiNbO<sub>3</sub>) [54–56] can be used to induce robust 1D confinement of neutral excitons in 1L-MoSe<sub>2</sub>, dominated by the Stark effect. LiNbO<sub>3</sub> is a very versatile ferroelectric material that can be integrated on oxide sacrificial layers using CMOS compatible processes to produce low loss waveguides [57] making it highly suitable for integrated optoelectronics and photonics [58–61]. Furthermore, periodically poled lithium niobate (PPLN) exhibits large surface charge densities within individual ferroelectric domains and atomically sharp Néel-type domain walls (DW) between domains [62–64]. Previously [65], we demonstrated that the in-plane electric field ( $E_x$ ) at the DWs establishes a potential landscape like a lateral  $p-n$  junction in 1L-TMDs when deposited on top of such domains. This potential induces 2D exciton drift and dissociation in the vicinity of the DW. The magnitude of  $E_x$  was shown to be up to  $E_x \sim 400$  V/ $\mu\text{m}$  and localized to

\* pedro.soubelet@wsi.tum.de

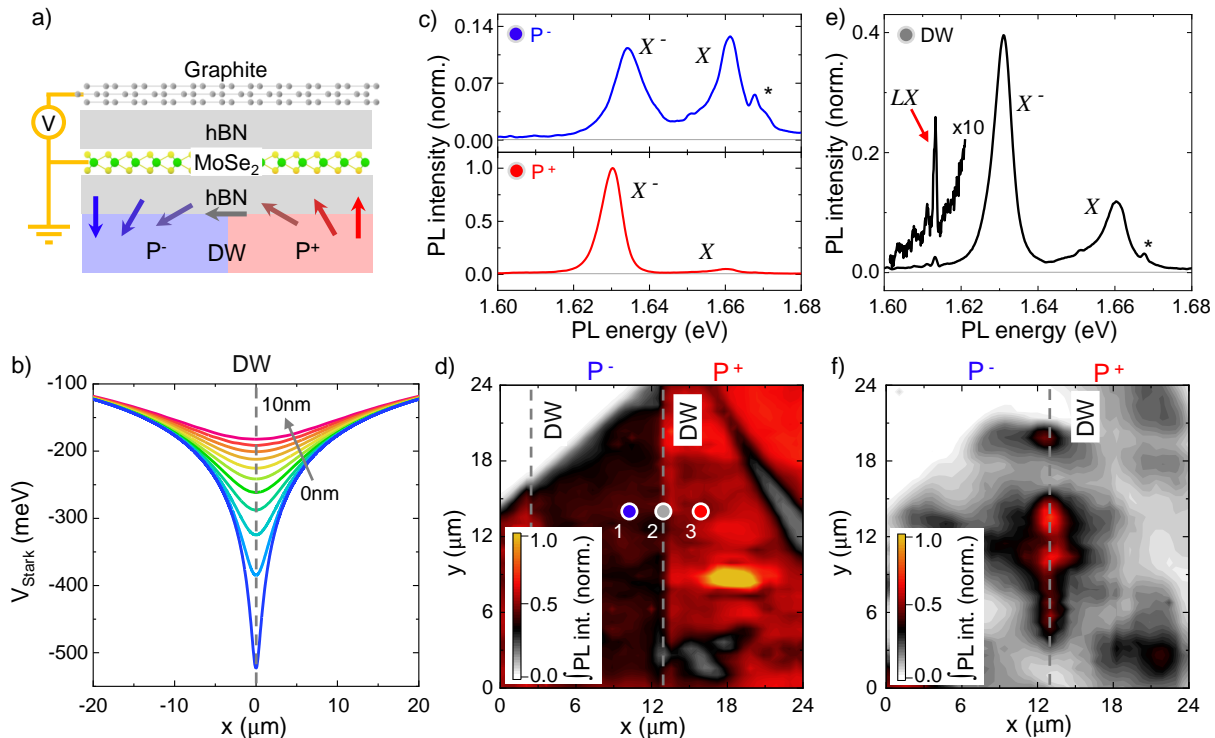


Figure 1. **Sample description and emission signatures of 1D confined excitons.** **a)** Schematic of the hBN-encapsulated 1L-MoSe<sub>2</sub> straddling DW boundaries in periodically poled LiNbO<sub>3</sub>. The red-to-blue arrows indicate the direction of the PPLN electric field near the DW, which generates a 1D trapping potential ( $V_{Stark}$ ). **b)** Calculated 1D trapping potential in the plane of the 1L-MoSe<sub>2</sub> for a variety of bottom hBN thicknesses. **c)**  $\mu$ PL spectra recorded at the  $P^-$  and  $P^+$  domains (top and bottom panels, respectively) showing the  $X$  and  $X^-$  emission. Features marked with an asterisk (\*) correspond to Raman lines from the substrate. **d)** False colour map showing the integrated PL across the sample. The spatial modulation reveals the underlying PPLN domains. Spots 1 and 3 mark the sites in which spectra in d) were acquired. **e)**  $\mu$ PL spectra recorded at the DW (spot 2 in d). In addition to the  $X$  and  $X^-$  emission, the spectra feature narrow emission lines ( $LX$ s) redshifted by  $\sim 50$  meV from  $X$ . **f)** False colour map showing the background subtracted and integrated PL intensity of the  $LX$ .

lengthscales of few nanometers, far beyond what can be achieved with metallic contacts. This suggests that DWs can serve as quantum traps for excitons via the DC Stark effect [52]. To validate this hypothesis, we performed spatially resolved micro-photoluminescence ( $\mu$ PL) experiments, PL-excitation and polarization resolved spectroscopy on hBN encapsulated 1L-MoSe<sub>2</sub> samples transferred on top of a PPLN substrate. Our results reveal the formation of 1D exciton states localized at the DW, with narrow emission lines that are redshifted by up to  $\sim 100$  meV from the MoSe<sub>2</sub> neutral exciton, depending on the sample structure. These observations are consistent with an exciton center-of-mass (COM) confined to lengthscales as small as  $\sim 3$  nm. The observed absence of interactions with surrounding free charges, combined with the thermal robustness observed through temperature-dependent PL experiments, suggests that proximal electric fields arising from ferroelectric DWs may be highly interesting for the exploration of strongly correlated exciton states [24].

## I. RESULTS AND DISCUSSION

Figure 1a shows a schematic of a van der Waals layered device, representative of those used in this study. The detailed structure of each device is provided in the Supplemental Material (SM) 1 VIII A. The devices were assembled via dry viscoelastic stamping techniques [66] and the design exploits the electric field at ferroelectric Néel-type DWs in LiNbO<sub>3</sub> [62, 67], depicted in Fig 1a by the rotating arrows. The large and nanometer scale in-plane electric field ( $E_x$ ) polarizes the TMD neutral exciton, resulting in a local reduction of the exciton transition energy and providing an attractive potential  $V_{Stark}$  within the 1L-MoSe<sub>2</sub> directly above the DW via the DC Stark effect [52],

$$V_{Stark} = -\frac{1}{2}\alpha E_x^2, \quad (1)$$

where  $\alpha = 6.5 \text{ nm}^2 \text{V}^{-2}$  [52] is the in-plane exciton polarizability of MoSe<sub>2</sub>. To estimate the in-plane electric field lengthscale and confinement potential, we calculated the electric field in the 1L-MoSe<sub>2</sub> plane as a function of

the bottom hBN thickness using finite element simulations. The resulting potentials are shown in Fig. 1b for a bottom hBN thickness varying from 0 nm to 10 nm and highlights the possibility to tune  $V_{Stark}$  by selecting the bottom hBN thickness. Further details on the simulations of the PPLN electric field and the trapping potential are provided in Section III and the SM 1 VIII A. To tune the electronic landscape in the TMD, the 1L-MoSe<sub>2</sub> was encapsulated in thin flakes of hexagonal boron nitride (hBN) and a top gate was incorporated to the structure by using a thin graphite flake. The Ohmic contact to the 1L-MoSe<sub>2</sub> was oriented across the DW to ensure that all regions of the sample are grounded, regardless of the junction potential.

We begin our investigation with spatially resolved low-temperature ( $T = 4.2$  K) PL spectroscopy on a sample with 8 nm thick bottom hBN (Sample 1). The sample was excited using a CW optical power  $P_{ex} = 1 \mu\text{W}$ , focused to a diffraction-limited spot of  $\sim 500$  nm ( $100\times$  objective,  $\text{NA} = 0.82$ ). The excitation photon energy was set to  $E_{ex} = 1.722$  eV,  $\sim 60$  meV above 1L-MoSe<sub>2</sub> neutral exciton ( $X$ ). Figure 1c shows selected PL spectra corresponding to two distinct domains with opposite out of plane ferroelectric polarization ( $P^-$  and  $P^+$ , respectively) [65]. The main difference between these spectra originates in the modulation of the free charge density across the domains. From the ratio of the trion ( $I_{X^-}$ ) to exciton ( $I_X$ ) intensities, we estimate a negative free charge density of  $n_{P^-} \simeq 0.9 \times 10^{10} \text{ cm}^{-2}$  and  $n_{P^+} \simeq 3.6 \times 10^{10} \text{ cm}^{-2}$  for the  $P^-$  and  $P^+$  domains, respectively [68]. Figure 1d shows a false-colour map of the integrated intensity of the 1L-MoSe<sub>2</sub> emission across the device. The spectra in Fig. 1c were obtained from the locations marked as “1” (blue dot) and “3” (red dot) in Fig. 1d. The PL intensity directly reflects the underlying PPLN structure, making the PL map an effective tool for identifying the ferroelectric domains. Based on the spatial modulation of the PL intensity, the ferroelectric polarization of each domain was determined in accordance with our previous work [65].

The key observation is shown in figure 1e where we plot the spectrum recorded directly at the DW (grey spot “2” in Fig. 1d) and reveals narrow emission lines ( $LX$ s) redshifted by  $\sim 50$  meV relative to  $X$ . We follow the spatial distribution of these emission features by integrating the 1L-MoSe<sub>2</sub> emission over the  $LX$  spectral range (1.595 eV to 1.615 eV), while subtracting the broad  $X^-$  emission as a background. The resulting map is shown in figure 1f, indicating that these spectrally narrow emission lines are macroscopically localized along the DW. For the remainder of this manuscript, we demonstrate that the  $LX$  emission is consistent with the radiative recombination of excitons confined in a 1D quantum trap at the DW.

The  $LX$ -emission lines were observed in a variety of samples with slightly different layer structure and Ohmic contacts. Figure 2a to c summarizes low-T  $\mu$ -PL line-cans across the DWs in three different samples (details in SM 2 VIII B). In each panel, the location of the DW

is indicated with a grey dashed line. The main difference between the samples is the bottom hBN thickness, as indicated in the panels. The PL of all samples show the neutral exciton emission  $X$ , the trion ( $X^-$ ) and, diffraction limited at the DW, the  $LX$  emission with an energy relative to  $X$  of  $\sim -50$  meV,  $\sim -70$  meV and  $\sim -120$  meV, for samples 1 to 3, respectively. The PL experiments performed on these samples show that by reducing the bottom hBN thickness, the emission energy of the  $LX$  redshifts with respect to  $X$ , directly showing the tunability of the confinement potential by controlling  $E_x$  in the plane of the 1L-MoSe<sub>2</sub>. To validate this result, we numerically solved the Schrödinger equation for the potential traps shown in Fig. 1b and obtained the wavefunctions and eigenenergies of the system (See SM3 VIII C for details). Figure 2d shows the calculated binding energy of the confined ground state in the quantum trap ( $\psi_0$ ) and the relative energy of the  $LX$ s with respect to the observed  $X$  energy. The overall trend follows the simulations, although the model overestimates the precise  $LX$  confinement. Specifically, the calculated binding energy is  $\sim 300$  meV higher for thin hBN thicknesses and  $\sim 100$  meV higher for hBN thicknesses  $> 5$  nm. This mismatch is possibly due to our oversimplified dielectric model, which is not valid for very thin hBN layers [69] and other systematic surface charge potentials, the detailed origin of which are beyond the scope of this work.

We continue the discussion of the 1D-nature of the  $LX$  states through the data obtained from sample 1 (8 nm bottom hBN), although similar results have been obtained from the other samples. In MoSe<sub>2</sub>, localized emission from defects occur within a similar energy range than the observed  $LX$  emission [70]. Therefore, we conducted power-dependent PL experiments to distinguish between those possibilities. Figure 3a shows selected PL spectra of the  $LX$  emission, by resonantly exciting  $X$  at  $E_{ex} = 1.66$  eV, with varying excitation power  $P_{ex}$  from 7 nW to 200  $\mu\text{W}$ . At very low  $P_{ex}$ , the spectrum is comprised of a single narrow emission line (linewidth  $\sim 400 \mu\text{eV}$ ,  $LX_0$ ) superimposed on a broad background. With increasing  $P_{ex}$ , the background develops some structure while maintaining its relative intensity with respect to the  $LX_0$  line. In addition, a few narrow peaks, spaced by  $\sim 3$  meV emerge from the noise floor that are blue detuned from  $LX_0$  (e.g.  $LX_1$ ). Figure 3b shows the integrated PL intensity of the distinct spectral features as a function of  $P_{ex}$ . Notably, the background,  $LX_0$ , and  $LX_1$  exhibit the same power-law dependence as the free trion, scaling approximately linear ( $s=0.97 \pm 0.01$ ). The absence of any saturation over more than five orders of magnitude of  $P_{ex}$  indicates that the  $LX$  emission is not defect-like [70].

Free excitons in TMDs exhibit circular optical selection rules [30, 71, 72], however, excitons confined within a 1D channel display a distinct behaviour. As previously reported, the long-range electron-hole exchange interaction mixes the exciton center-of-mass (COM) motion with the  $K/K'$ -valley degrees of freedom [33, 50, 73]. The mo-

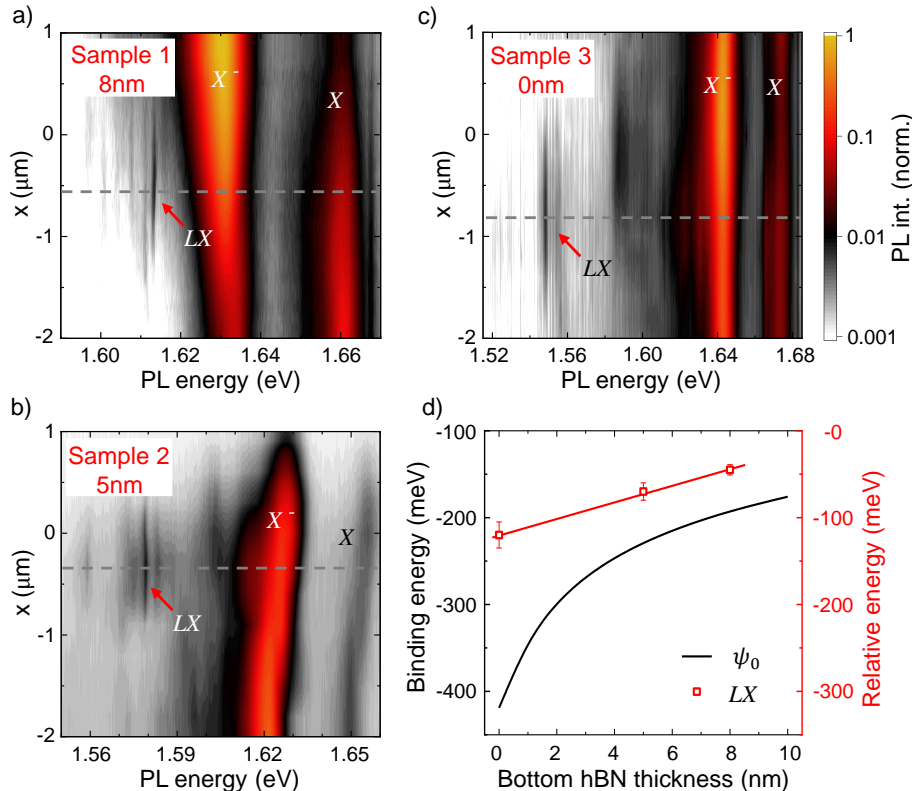


Figure 2. **PL experiments across samples with different bottom hBN thickness** a), b) and c) False-color plot of the 1L-MoSe<sub>2</sub> emission across the DW for three different samples. Sample 1 is a 1L-MoSe<sub>2</sub> stacked on top of 8 nm thick hBN, Sample 2 a 1L-MoSe<sub>2</sub> stacked on top of 5 nm thick hBN, and sample 3 is a 1L-MoSe<sub>2</sub> directly stacked on top of the PPLN. The grey dotted line marks the DW position d) Comparison between the theoretical binding energy of the first confined state ( $\psi_0$ ) and the experimentally observed localized states ( $LX$ ) energy relative to the  $X$  energy for the three samples. The red line over the experimental data serves as a guide to the eye.

tional in-plane anisotropy from the 1D trapping potential leads to the splitting of the confined exciton COM wavefunctions into orthogonal linearly polarized states, parallel or perpendicular to the DW. Consequently, the energy of the  $n^{\text{th}}$  quantized state splits into two components, one with linear polarization parallel to the DW and energy  $E_n$ , and a second linearly polarized perpendicular to the DW and energy  $E_n^\perp = E_n + \delta_n$ . Here,  $\delta_n = \gamma k_n$ , where  $\gamma$  is the exchange-interaction coupling parameter and  $k_n$  the average COM wavevector of the state [50, 73, 74].

Motivated by this expectation, we performed polarization-resolved colinear excitation-collection PL spectroscopy on the localized exciton peaks at the DW. Figure 3c shows a false-color plot of the background subtracted  $LX$ s emission as a function of the excitation-emission angle measured relative to the direction parallel to the DW. The  $LX_0$  and  $LX_1$  states exhibit a clear linear polarization parallel to the DW, with significantly reduced emission perpendicular to the DW. Figure 3d shows the extracted intensity of  $LX_0$  and  $LX_1$  as a function of the excitation-collection angle, solid lines correspond to sinusoidal fits to the

data. Both  $LX_0$  and  $LX_1$  display intensity suppression in the direction perpendicular to the DW of  $\sim 50\%$  and  $\sim 40\%$ , respectively. This behaviour is consistent with previous observations of 1D confined excitons in TMDs [33, 50], although the degree of suppression observed here is comparatively lower. The absence of emission in the direction perpendicular to the DW aligns with previous reports of 1D states. As the confinement increases, the corresponding  $k_n$  increases, shifting states with perpendicular polarization to higher energies, thereby rendering their occupation unfavourable and eventually suppressing their emission [33]. In contrast, the background emission shows a significantly smaller modulation in its intensity and, in the case of the lower energy emission component, a spectral shift (see Fig. 3c). The polarization-resolved behaviour of the background shows a clearly different behavior as the  $LX$ . While a precise identification of these background states remains unclear and demands further understanding, they may stem from strain, local dielectric fluctuations, or structural imperfections, which modulate the 1D-trapping potential along the DW.

To explore the 1D-exciton levels and their relationship

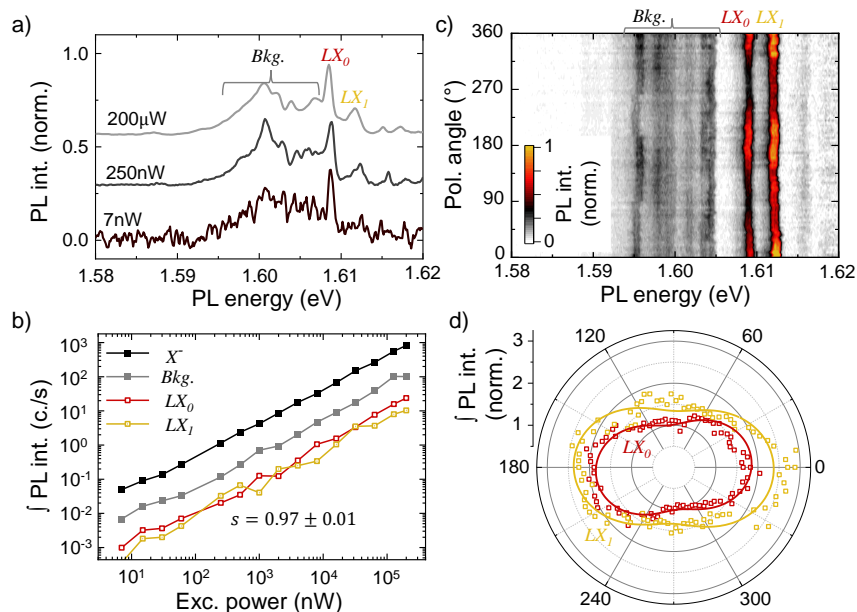


Figure 3. **Power-dependency and linearly polarized emission of 1D confined states.** **a)** Tron-subtracted  $LX$  PL spectra in resonance under varying excitation powers, 7 nW, 250 nW, and 200  $\mu$ W. **b)** Integrated intensity of  $X^-$ , Background (Bck.), and individual  $LX$ s as a function of excitation power. The intensity follows a power-law dependence with an exponent  $s = 0.97 \pm 0.05$ . **c)** False-color plot of the background-subtracted in resonance  $LX$  PL spectra as a function of the excitation-collection linear polarization angle. **d)** Polar plot of the PL spectral intensity at the central position of individual  $LX$ s as a function of excitation-collection linear polarization angle. Solid lines are a sinusoidal fit.

with the 2D counterpart, we conducted PL-excitation (PLE) experiments. Figure 4a shows a false-colour plot of the  $LX$  PL spectra as a function of  $E_{ex}$ . All features in this spectral range exhibit a strong resonance when exciting near the  $X$  energy at  $\sim 1.66$  eV, indicated by the grey horizontal line. No resonance is observed when the excitation laser energy is swept across the  $X^-$ . Figure 4b shows the integrated PL intensity of the spectral lines (arrows in Fig.4a) as a function of excitation energy. Resonant excitation of the  $X$  increases the  $LX$ s emission by two orders of magnitude as compared to non-resonant excitation. This shows that the most efficient way to optically excite the 1D channel is by generating a 2D exciton population which is subsequently trapped at the DW. Notably, even while exciting the sample at  $E_{ex} = 1.62$  eV,  $\sim 10$  meV above  $LX_0$ , there is no increase in the emission intensity of any features. This observation suggests two possible explanations, the relatively small area of the 1D channel compared to the overall laser beam size, and the inherently lower oscillator strength of polarized excitons relative to  $X$ .

To investigate the thermal robustness of the 1D confined states, we performed temperature dependent PL. Figure 4c shows temperature-dependent PL spectra, from  $T = 4.7$  K to 60 K, while exciting the sample resonantly with the  $X$  energy. The  $X^-$  emission remains unaffected in both intensity and spectral position until the temperature reaches approximately 40 K. Beyond this point, increasing temperature causes the  $X^-$  to notably redshift and decrease in intensity, consistent with previ-

ous reports [75]. In contrast, the intensity of the  $LX$ s and the background gradually decrease, with a sudden variation above 30 K. Figure 4d presents the extracted intensities of  $LX_0$ ,  $LX_1$ , and the background as a functions of  $1/T$ . The temperature dependence of each feature  $[I(T)]$  is fitted with a modified Arrhenius equation that incorporates two activation energies,  $E_1$  and  $E_2$ :

$$I(T) = \frac{I_0}{1 + Ae^{(-E_1/k_B T)} + Be^{(-E_2/k_B T)}}, \quad (2)$$

where  $A$  and  $B$  are amplitude parameters. The fitting procedure yields a first activation energy of  $E_1 \sim 2$  meV for all features, which governs the intensity evolution at low temperatures. The second activation energy is determined to be  $47 \pm 4$  meV,  $40 \pm 5$  meV, and  $32 \pm 5$  meV for the background,  $LX_0$ , and  $LX_1$  features, respectively. Notably, in all cases, the second activation energy closely matches the energy difference to the  $X$  and not the nearby  $X^-$ , indicating the activation of a scattering mechanism that facilitates the transition of these localized states into the 2D continuum.

Lastly, we analyzed the influence of free charges on the  $LX$  features by tuning the electron density in the sample via the top gate (see Fig. 1a). The effect of the charge density is characterized through the parameter  $\Gamma = I_{X^-}/(I_{X^-} + I_X)$ , where  $I_{X^-}$  ( $I_X$ ) is the trion(exciton) intensity. Therefore, in a charge neutrality condition,  $\Gamma \rightarrow 0$  since  $I_{X^-} \rightarrow 0$ . On the other hand, by increasing the free charge density,  $\Gamma \rightarrow 1$  since  $I_X \rightarrow 0$ . The effect of the top gate is summarized by the

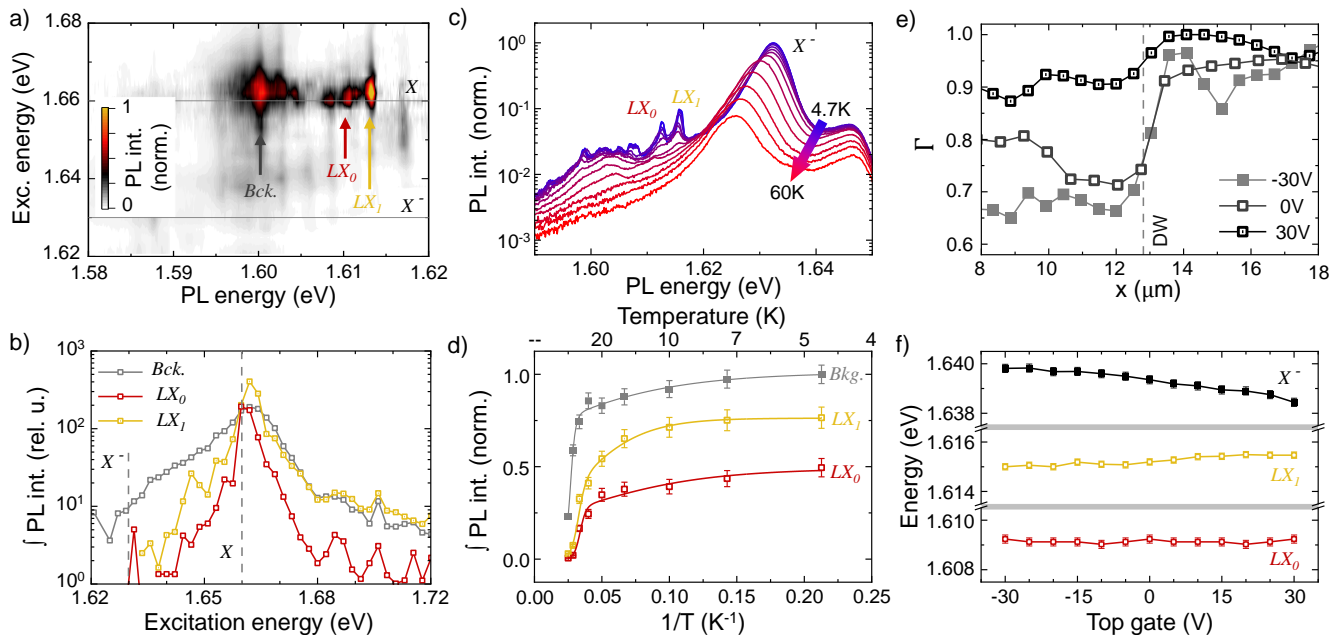


Figure 4. **Resonance effects, temperature evolution and free charge density effects on the 1D confined states.** **a)** False-colour plot of the trion-subtracted  $LX$  PL spectra as a function of the excitation energy revealing the resonance with  $X$ . **b)** Integrated PL spectral intensity as function of the excitation energy. **c)** In resonance  $LX$ s and trion PL spectra as a function of temperature, from 4.7K to 60K. **d)** Integrated PL intensity as a function of  $1/T$ . Solid lines correspond to a modified Arrhenius fitting. **e)** Line scan showing the top gate voltage effect on the 1L-MoSe<sub>2</sub> photophysics described through the parameter  $\Gamma = I_{X^-}/(I_{X^-} + I_X)$ . **f)**  $X^-$ ,  $LX_0$  and  $LX_1$  spectral position as a function of the top gate voltage.

line scans in Figure 4e, which show  $\Gamma$  in the vicinity of the DW for three selected voltages (for further details, see SM VIII D). While the 1L-MoSe<sub>2</sub> is uniformly gate-biased, the effect of the charging is notably portrayed by the behavior of  $\Gamma$  on the  $P^-$  domain. Figure 4f shows the extracted spectral position for  $LX_0$ ,  $LX_1$  and  $X^-$  as a function of the top gate voltage at the DW. The trion feature redshifts by  $\sim 2$  meV throughout the top gate voltage range, consistent with the behavior of repulsive polarons with increasing the 2D Fermi level [68]. Meanwhile, the  $LX$ s spectral position remains nearly constant, indicating that the trapping potential is unaffected by the free charge density. This behaviour contrasts the work on gate-induced exciton confinement [33, 50] where the effective trapping potential is a combination of Stark effect and interaction-induced confinement, which depends on the free carrier density. Therefore, the confinement potential in our platform is not a result of many-body interactions and is, consequently, insensitive to variations in the local free charge density.

We conclude by discussing the length scales of the confinement potential. Our calculations (see Fig. 1b) show that the maximum confinement energy for an encapsulated 1L-MoSe<sub>2</sub> sample with an 8 nm thick bottom hBN is  $-200$  meV relative to  $X$  (see SM 3 VIII C for details). However, as discussed above,  $LX$ s in this device are redshifted by only  $-50$  meV. This difference suggest that the built-in electric field generated by the  $p-n$  homojunction at the DW diminishes  $V_{Stark}$  and

results in a shallower effective potential  $V_{eff}$ . Therefore, to calculate the confined COM wavefunctions, we rescale  $V_{Stark}$  to a depth of 50 meV while preserving its overall profile. By numerically solving the Schrödinger equation for  $V_{eff}$  using a total exciton effective mass  $m_X = 1.29m_0$ , where  $m_0$  is the electron mass [76], we obtained the wavefunctions and eigenenergies of the system (see SN 3 VIII C for details). The COM confinement, defined as  $\ell_n = \sqrt{\langle \psi_n | x^2 | \psi_n \rangle}$ , yields  $\ell_0 = 3.0$  nm and  $\ell_1 = 5.6$  nm for the ground and first excited confined states, with an energy separation of  $\Delta E = 4.5$  meV. Assuming the experimentally observed spectral features  $LX_0$  and  $LX_1$  corresponds to these states, the measured value of  $\Delta E \sim 3.5$  meV, which slightly depends on the specific position along the DW, is in good agreement with theoretical expectations. Using this experimental  $\Delta E = \hbar\omega$  within an harmonic confinement potential approximation, we estimate the COM confinement length-scale to be  $\ell_n = \sqrt{\frac{\hbar}{m_X\omega} (n + \frac{1}{2})}$ , yielding  $\ell_0 = 2.9$  nm and  $\ell_1 = 5.0$  nm. Notably, both the harmonic approximation and the numerical estimation of  $V_{eff}$  yield similar COM confinement values. More important, our device structure effectively decouples the 1D exciton state from the 2D counterpart by providing a potential trap that, compared to prior studies [33, 50], is an order of magnitude higher with a  $\sim 50\%$  smaller COM confinement length.

## II. CONCLUSIONS

In summary, we fabricated optoelectronic devices that leverage the large in-plane electric field gradients at the PPLN DWs to confine 1L-MoSe<sub>2</sub> neutral excitons within a 1D channel. Spatially resolved  $\mu$ -PL experiments revealed narrow emission lines at the DW, redshifted from the neutral 1L-MoSe<sub>2</sub> exciton. These emission lines appear diffraction-limited in the direction perpendicular to the DW while extend macroscopically along the DW. Complementary power-dependent PL, linearly polarized PL, PLE, and temperature dependent PL spectroscopy suggest that these emission lines are consistent with the formation of a 1D exciton gas at the DW. Although our design currently lacks a mechanism to fine-tune the confinement potential in-situ, the proper selection of the bottom hBN layer thickness allows manipulation of the confinement potential by up to  $\sim 100$  meV, as demonstrated in a sequence of samples. This is an order-of-magnitude enhancement as compared to previous reports [33, 50]. This robust confinement effectively decouples the 1D exciton state from its 2D counterpart and suppresses many-body interactions with the environment outside the 1D channel. As a result, our platform offers a compelling system for manipulating and localizing excitons in TMDs, enabling the future exploration of 1D exciton dynamics as well as highly correlated phases of 1D-dipolar exciton gases [18, 19, 22, 24].

## III. METHODS

### A. Sample Fabrication

The periodically poled domains were fabricated by bulk electric field poling of commercial  $500\mu\text{m}$  thick congruent  $z$ -cut LiNbO<sub>3</sub> crystals. The quality of the poling was verified optically, which allows us to visualize the domain pattern and evaluate its uniformity without any surface contamination or disruption [77]. Furthermore, reference PPLN samples fabricated in the same batch were etched for 10 min in HF acid to convert the PPLN pattern into a surface relief grating (due to the differential etching of  $-z$  and  $+z$  domains in HF), further confirming the successful domain inversion on both faces with a domain duty cycle close to 50% on the lithographically patterned face of the sample (originally  $-z$ ).

Monolayers MoSe<sub>2</sub>, hBN flakes and few layers graphene were obtained from commercial bulk crystals via mechanical exfoliation. We specifically selected 1L-MoSe<sub>2</sub> due

to its lack of dark states below the  $X$  energy and the simplicity of its PL spectra at low temperature, therefore facilitating the identification of additional emission features that result from the 1D  $X$  confinement.

All the samples used in this work were stacked and encapsulated between thin hBN flakes using dry transfer techniques based on polycarbonate films, similar to Ref. 66.

### B. Optical experiments

All experiments were conducted using a helium exchange gas cryostat, equipped with a cryogenically compatible objective (numerical aperture  $NA = 0.82$ ) and a temperature controller. The excitation source was a CW tunable Ti:Sa laser.

## IV. ACKNOWLEDGEMENTS

We gratefully acknowledge the German Science Foundation (DFG) for financial support via the SPP-2244 (DI 2013/5-1, FI 947/7-2, FI 947/7-1 and FA 971/8-1) the clusters of excellence MCQST (EXS-2111) and e-conversion (EXS-2089). P.S. acknowledges the financial support from the DFG through the Walter Benjamin program.

## V. AUTHOR CONTRIBUTION

P.S., A.V.S., and J.J.F. conceived the project and K.G. provided the PPLN substrates. P.S. modeled the system and developed the calculations with the participation of A.A.H. P.S. designed the samples, which were fabricated by P.S., Y.T., and P.J. P.S., Y.T. and A.A.H. performed the optical measurements, and P.S. and Y.T. analyzed the data. P.S. and A.V.S. wrote the paper with input from all coauthors. All authors reviewed the manuscript.

## VI. DATA AVAILABILITY

The data that support the findings of this study are available on request from the corresponding author.

## VII. COMPETING INTERESTS

The Authors declare no Competing Financial or Non-Financial Interests.

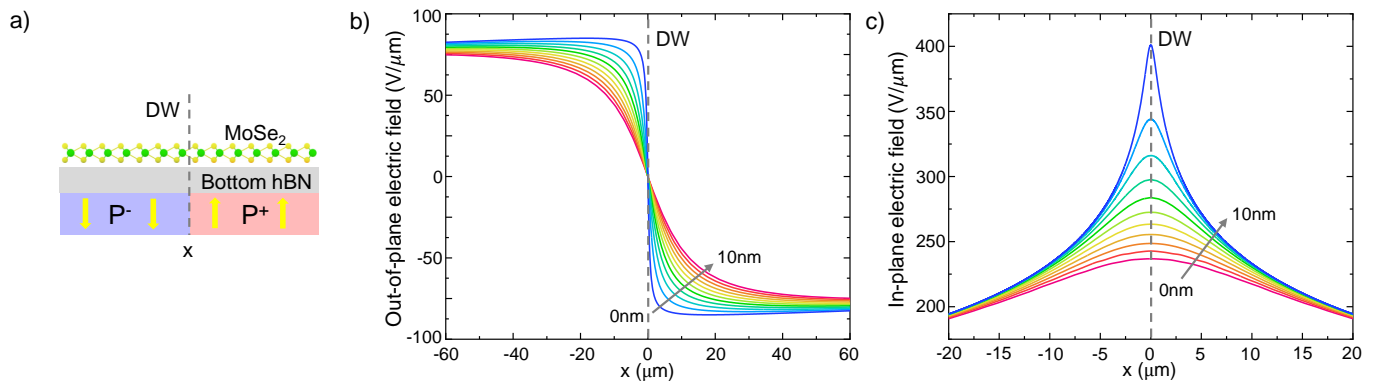


Figure 5. **Calculated electric field at the DW as a function of the bottom hBN.** a) Schematic representation of the bottom hBN flake and MoSe<sub>2</sub> monolayer used to calculate the electric field at the PPLN DW. b) Calculated out-of plane electric field component. c) Calculated in-plane electric field component.

## VIII. SUPPLEMENTARY MATERIAL

### A. Determination of the electric field at the domain wall

Figure 5a displays a schematic representation of the PPLN substrate, the bottom hBN flake and the monolayer 1L-MoSe<sub>2</sub> used to estimate the electric field at the TMD position. Figures 5b and c present the out-of-plane and the in-plane electric field at the TMD monolayer position as a function of the bottom hBN used for the sample encapsulation. The calculations were produced by finite elements assuming an hBN refractive index of  $n_{hBN} = 1.8$  and an effective surface charge density on the PPLN domains of  $\pm 2.7 \mu\text{C}/\mu\text{m}^2$  as determined in our previous work [65].

Note that, by grounding the samples, the reordering of charges screens the electric field along all domains, except the in-plane electric field at the DW, where the device behaves like a nanometer scale  $p-n$  homojunction generating a build in electric field that reduces  $V_{Stark}$  resulting in an effective potential  $V_{eff}$ .

### B. Observation of sharp emission lines associated to 1D confined excitons in different samples

The observation of sharp emission lines attributed to localized exciton states was consistently reproduced across multiple samples. The results are summarized in Figure 6, which presents data from three distinct samples. Specifically, Figs. 6a, d, and g displays the optical micrograph of each device, with the green lines marking the contour of the 1L-MoSe<sub>2</sub> and a vertical black line marking the DW on each sample. Additionally, below each optical picture, a schematic representation shows the sample architecture. Figs. 6b, e, and h presents the false-color plot of their PL (samples in Figs. 6b, e, and h, respectively) across the DW and along the red arrows depicted in their micrographs. Finally, Figs. 6c, f, and i present, for each device in Figs. 6a, d, and g, respectively, the PL spectra at the DW. The energy scale in these figures is relative to the 2D neutral exciton.

The 1L-MoSe<sub>2</sub> flake in the sample of Fig. 6a correspond to the grounded sample presented in the main text, it was stacked with 8 nm bottom hBN, and its false color plot in Fig. 6b and its PL in c display  $LX$ s emission redshifted by  $\sim 50$  meV from the exciton feature. The sample in Fig. 6d has 5 nm bottom hBN and was not grounded. As a result,  $X$  and  $X^-$  spectrally shift due to the out-of-plane electric field that is not completely screened and produces Stark shift. Its false colour plot in Fig. 6e and its PL in f show the  $LX$ s redshifted by  $\sim 70$  meV from the exciton feature. The last sample, displayed in Fig. 6g was directly stacked on top of the PPLN and was grounded. Its false colour plot in Fig. 6h and the spectra i display the exciton and trion features and,  $\sim 120$  meV redshifted from the exciton, the localized states.

Our results across different samples show that it is possible to tune the 1D confinement by properly selecting the bottom hBN thickness in the device structure (see next section for details).



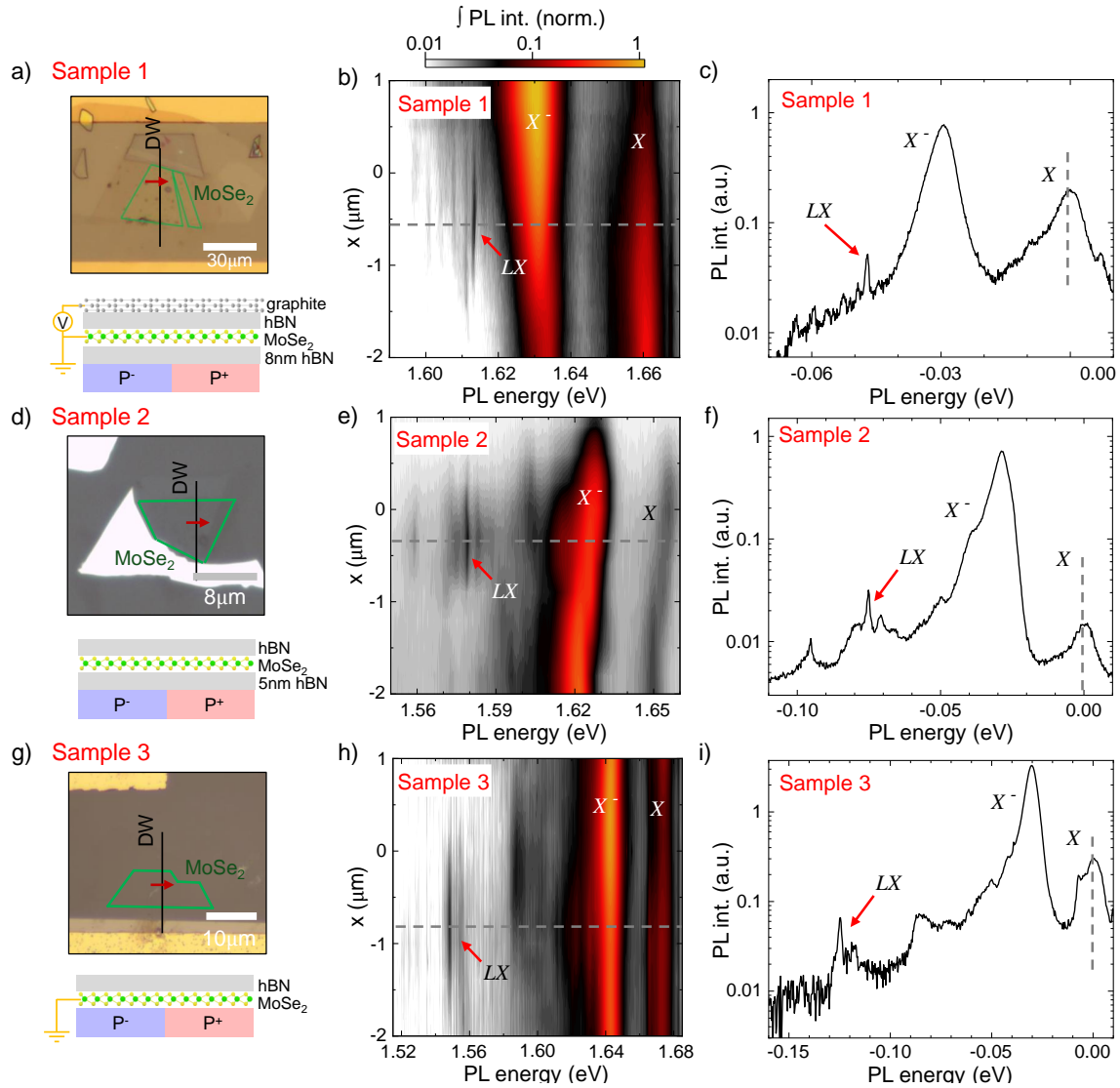


Figure 6. **PL experiments on different samples.** a) Optical micrograph and schematic representation of the 1L-MoSe<sub>2</sub> sample presented in the main text and that was stacked on top of 5 nm bottom hBN flake. b) False-colour plot of the integrated PL intensity across the DW for the sample in a. c) PL spectra at the DW for the sample in a. d) Optical micrograph of a 1L-MoSe<sub>2</sub> stacked on the PPLN with a 5 nm bottom hBN flake. e) False-colour plot of the PL intensity across the DW for the sample in d. f) PL spectra at the DW for the sample presented in d. g) Optical micrograph of a grounded 1L-MoSe<sub>2</sub> stacked directly on the PPLN. h) False-colour plot presenting the PL intensity across the DW for the sample in g. i) PL spectra at the DW for the sample in g. The PL spectra in c, f and i are presented on an energy scale relative to the 2D neutral exciton.

### C. Eigenfunctions and eigenenergies of the 1D device

Using an in-plane exciton polarizability for 1L-MoSe<sub>2</sub> of  $\alpha = 6.5 \text{ nm}^2 \text{ V}^{-2}$  [52] and the calculated  $E_x(x)$  (see Fig. 5c), we determined the theoretical potential  $V_{Stark}(x)$  presented in figure 7a. By numerically solving the Schrödinger equation for this DC Stark potential trap, we obtained the wavefunctions and eigenenergies of the system, assuming an exciton mass of  $1.2895m_0$ , where  $m_0$  is the electron mass [76]. The eigenenergies for the first confined states ( $\psi_0$  to  $\psi_5$ ) are plotted in figure 7b as a function of the bottom hBN thickness. The inset in Fig. 7b illustrates the wavefunctions for the first confined states for a sample stacked on top of 4 nm bottom hBN.

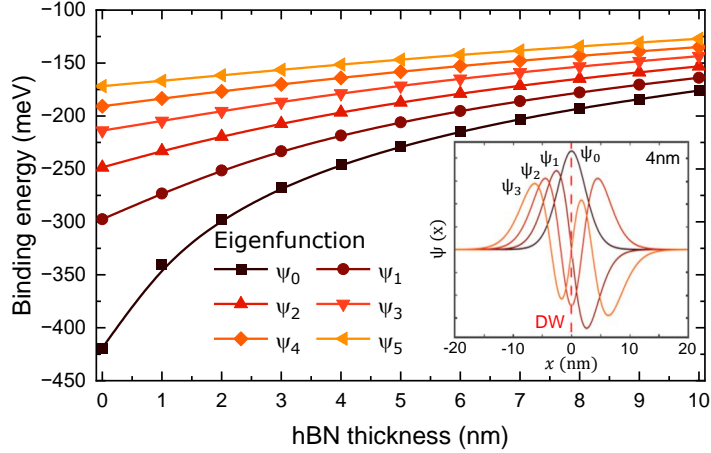


Figure 7. **Potential trap and confined states.** Theoretical calculation of the eigenenergies of the confined states as a function of the bottom hBN thickness. Inset: First wavefunctions for a sample stacked on 4 nm hBN.

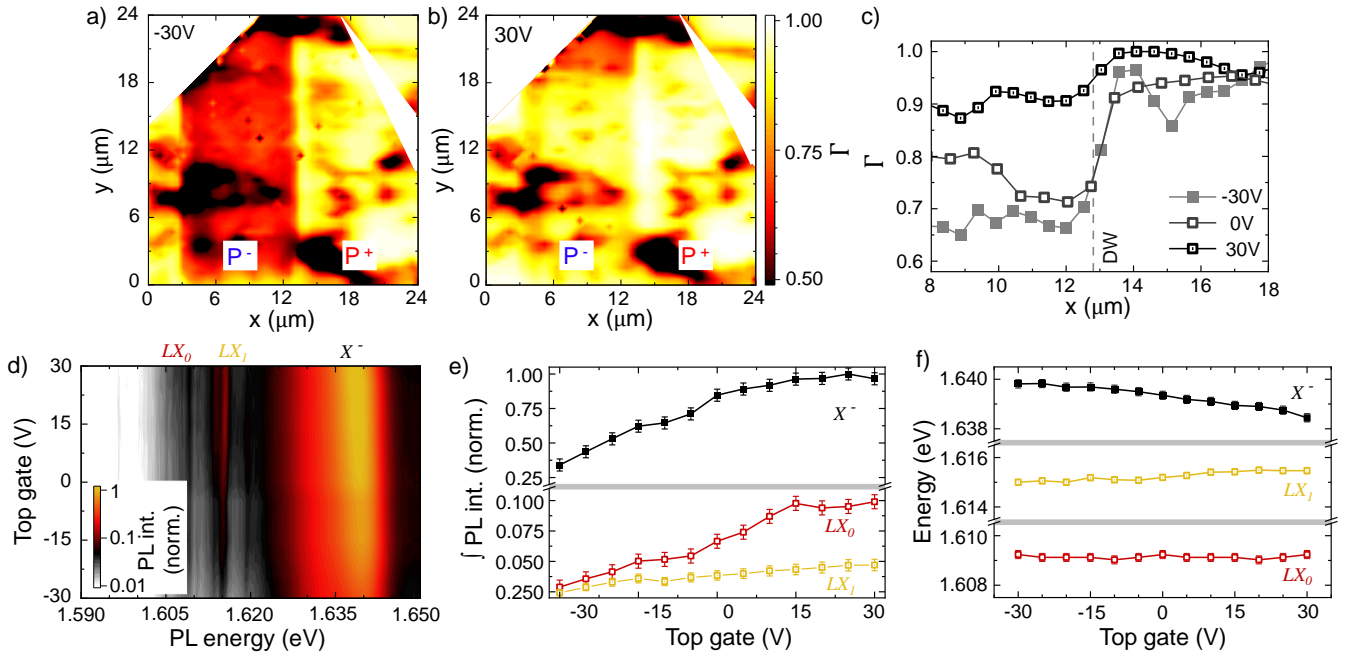


Figure 8. **Electronic landscape effect over LXs.** **a** and **b**) False colour maps showing the top gate effect over the MoSe<sub>2</sub> photophysics through the parameter  $\Gamma = I_{X^-}/(I_{X^-} + I_X)$ . **c**)  $\Gamma$  modulation across the DW for different top gate voltages. **d**) False colour plot of the  $LX$  and trion PL spectra in resonance as a function of the top gate. **e**)  $X^-$ ,  $LX_0$  and  $LX_1$  intensity as a function of the top gate voltage. **f**)  $X^-$ ,  $LX_0$  and  $LX_1$  spectral position as a function of the top gate.

#### D. Electronic landscape effects over LXs

while a comprehensive investigation of the material response lies beyond the scope of this work, we analyzed the influence of the free charge density on the  $LX$  emission by tuning the sample top gate (sample 1). To characterize the effect of the top gate on the photophysics of the 2D counterpart, we introduce the parameter  $\Gamma = I_{X^-}/(I_{X^-} + I_X)$ . Figure 4a and b present false-colour maps of  $\Gamma$  across the sample under top gate voltage of -30 V and 30 V, respectively. At -30 V, the  $P^-$  and  $P^+$  domains exhibit distinctly different charge density, reflected by  $\Gamma \simeq 0.65$  for the  $P^-$  domain and  $\Gamma \simeq 0.95$  for the  $P^+$  domain. In contrast, the map at 30 V reveals a much more homogeneous  $\Gamma$  across the sample. Note that as  $\Gamma \rightarrow 1$ , the  $X$  emission is suppressed. The effect of the top gate is summarized in Figure 4c, which presents  $\Gamma$  across the DW for three different voltages. Figure 4d presents a false-colour plot of the in-resonance PL at

the DW as function of the top gate voltage. Sweeping the top gate in the positive direction increases  $X^-$  intensity and induces a redshift of 2 meV, consistent with previous reports [68]. While the  $X$  emission is suppressed by increasing the charge density at positive voltages, the  $LX$ s emission increases. Figure 4e and f show the extracted intensity and spectral position for  $LX_0$ ,  $LX_1$  and  $X^-$  as a function of the top gate voltage. While  $LX$ s and  $X^-$  increase their intensity with similar proportion, the spectral position of  $LX_0$  and  $LX_1$  remains nearly constant, displaying a slight blueshift of  $\sim 0.5$  meV.

- 
- [1] G. Bastard, *Wave mechanics applied to semiconductor heterostructures* (New York, NY (USA); John Wiley and Sons Inc., 1990).
- [2] B. W. Baugher, H. O. Churchill, Y. Yang, and P. Jarillo-Herrero, *Nature nanotechnology* **9**, 262 (2014).
- [3] C. Palacios-Berraquero, D. M. Kara, A. R.-P. Montblanch, M. Barbone, P. Latawiec, D. Yoon, A. K. Ott, M. Loncar, A. C. Ferrari, and M. Atatüre, *Nature communications* **8**, 15093 (2017).
- [4] A. Branny, S. Kumar, R. Proux, and B. D. Gerardot, *Nature communications* **8**, 15053 (2017).
- [5] H. Baek, M. Brotons-Gisbert, Z. X. Koong, A. Campbell, M. Rambach, K. Watanabe, T. Taniguchi, and B. D. Gerardot, *Science advances* **6**, eaba8526 (2020).
- [6] M. Fogler, L. Butov, and K. Novoselov, *Nature communications* **5**, 4555 (2014).
- [7] D. Unuchek, A. Ciarrocchi, A. Avsar, K. Watanabe, T. Taniguchi, and A. Kis, *Nature* **560**, 340 (2018).
- [8] K. L. Seyler, P. Rivera, H. Yu, N. P. Wilson, E. L. Ray, D. G. Mandrus, J. Yan, W. Yao, and X. Xu, *Nature* **567**, 66 (2019).
- [9] Y. Shimazaki, I. Schwartz, K. Watanabe, T. Taniguchi, M. Kroner, and A. Imamoglu, *Nature* **580**, 472 (2020).
- [10] L. Wang, E.-M. Shih, A. Ghiotto, L. Xian, D. A. Rhodes, C. Tan, M. Claassen, D. M. Kennes, Y. Bai, B. Kim, *et al.*, *Nature materials* **19**, 861 (2020).
- [11] Y. Xu, S. Liu, D. A. Rhodes, K. Watanabe, T. Taniguchi, J. Hone, V. Elser, K. F. Mak, and J. Shan, *Nature* **587**, 214 (2020).
- [12] Y. Tang, L. Li, T. Li, Y. Xu, S. Liu, K. Barmak, K. Watanabe, T. Taniguchi, A. H. MacDonald, J. Shan, *et al.*, *Nature* **579**, 353 (2020).
- [13] E. C. Regan, D. Wang, C. Jin, M. I. Bakti Utama, B. Gao, X. Wei, S. Zhao, W. Zhao, Z. Zhang, K. Yumigeta, *et al.*, *Nature* **579**, 359 (2020).
- [14] X. Huang, T. Wang, S. Miao, C. Wang, Z. Li, Z. Lian, T. Taniguchi, K. Watanabe, S. Okamoto, D. Xiao, *et al.*, *Nature Physics* **17**, 715 (2021).
- [15] T. Li, S. Jiang, B. Shen, Y. Zhang, L. Li, T. Devakul, K. Watanabe, T. Taniguchi, L. Fu, J. Shan, and K. F. Mak, *Nature* **600**, 641 (2021).
- [16] P. Wang, G. Yu, Y. H. Kwan, Y. Jia, S. Lei, S. Klemen, F. A. Cevallos, R. Singha, T. Devakul, K. Watanabe, T. Taniguchi, S. L. Sondhi, R. J. Cava, L. M. Schoop, S. A. Parameswaran, and S. Wu, *Nature* **605**, 57 (2022).
- [17] A. J. Campbell, M. Brotons-Gisbert, H. Baek, V. Vitale, T. Taniguchi, K. Watanabe, J. Lischner, and B. D. Gerardot, *npj 2D Materials and Applications* **6**, 79 (2022).
- [18] I. Carusotto, D. Gerace, H. Tureci, S. De Liberato, C. Ciuti, and A. Imamoglu, *Physical review letters* **103**, 033601 (2009).
- [19] D. W. Hallwood, T. Ernst, and J. Brand, *Physical Review A—Atomic, Molecular, and Optical Physics* **82**, 063623 (2010).
- [20] I. Carusotto and C. Ciuti, *Reviews of Modern Physics* **85**, 299 (2013).
- [21] C. Noh and D. G. Angelakis, *Reports on Progress in Physics* **80**, 016401 (2016).
- [22] J. Schloss, A. Benseny, J. Gillet, J. Swain, and T. Busch, *New Journal of Physics* **18**, 035012 (2016).
- [23] D. M. Kennes, M. Claassen, L. Xian, A. Georges, A. J. Millis, J. Hone, C. R. Dean, D. Basov, A. N. Pasupathy, and A. Rubio, *Nature Physics* **17**, 155 (2021).
- [24] R. Oldziejewski, A. Chiocchetta, J. Knörzer, and R. Schmidt, *Physical Review B* **106**, L081412 (2022).
- [25] K. F. Mak, C. Lee, J. Hone, J. Shan, and T. F. Heinz, *Physical review letters* **105**, 136805 (2010).
- [26] A. Splendiani, L. Sun, Y. Zhang, T. Li, J. Kim, C.-Y. Chim, G. Galli, and F. Wang, *Nano letters* **10**, 1271 (2010).
- [27] D. Xiao, G.-B. Liu, W. Feng, X. Xu, and W. Yao, *Physical review letters* **108**, 196802 (2012).
- [28] K. F. Mak, K. He, C. Lee, G. H. Lee, J. Hone, T. F. Heinz, and J. Shan, *Nature materials* **12**, 207 (2013).
- [29] A. V. Stier, K. M. McCreary, B. T. Jonker, J. Kono, and S. A. Crooker, *Nature communications* **7**, 10643 (2016).
- [30] G. Wang, A. Chernikov, M. M. Glazov, T. F. Heinz, X. Marie, T. Amand, and B. Urbaszek, *Reviews of Modern Physics* **90**, 021001 (2018).
- [31] A. V. Stier, N. P. Wilson, K. A. Velizhanin, J. Kono, X. Xu, and S. A. Crooker, *Physical review letters* **120**, 057405 (2018).
- [32] M. Goryca, J. Li, A. V. Stier, T. Taniguchi, K. Watanabe, E. Courtade, S. Shree, C. Robert, B. Urbaszek, X. Marie, *et al.*, *Nature communications* **10**, 4172 (2019).
- [33] D. Thureja, A. Imamoglu, T. Smoleński, I. Amelio, A. Popert, T. Chervy, X. Lu, S. Liu, K. Barmak, K. Watanabe, *et al.*, *Nature* **606**, 298 (2022).
- [34] L. Zhang, F. Wu, S. Hou, Z. Zhang, Y.-H. Chou, K. Watanabe, T. Taniguchi, S. R. Forrest, and H. Deng, *Nature* **591**, 61 (2021).
- [35] S. Susarla, M. H. Naik, D. D. Blach, J. Zipfel, T. Taniguchi, K. Watanabe, L. Huang, R. Ramesh, F. H. da Jornada, S. G. Louie, *et al.*, *Science* **378**, 1235 (2022).
- [36] C. Qian, M. Troue, J. Figueiredo, P. Soubelet, V. Villafañe, J. Beierlein, S. Klembt, A. V. Stier, S. Höfling, A. W. Holleitner, *et al.*, *Science Advances* **10**, eadk6359 (2024).
- [37] M. R. Rosenberger, C. K. Dass, H.-J. Chuang, S. V. Sivaram, K. M. McCreary, J. R. Hendrickson, and B. T. Jonker, *ACS nano* **13**, 904 (2019).
- [38] M. Kremser, M. Brotons-Gisbert, J. Knörzer, J. Gückelhorn, M. Meyer, M. Barbone, A. V. Stier, B. D. Gerardot, K. Müller, and J. J. Finley, *npj 2D Materials and Applications* **4**, 8 (2020).

- [39] Y. Bai, L. Zhou, J. Wang, W. Wu, L. J. McGilly, D. Halbertal, C. F. B. Lo, F. Liu, J. Ardelean, P. Rivera, *et al.*, *Nature Materials* **19**, 1068 (2020).
- [40] L. Yu, M. Deng, J. L. Zhang, S. Borghardt, B. Kardynal, J. Vuckovic, and T. F. Heinz, *Nano Letters* **21**, 2376 (2021).
- [41] M. Kögl, P. Soubelet, M. Brotons-Gisbert, A. Stier, B. Gerardot, and J. Finley, *npj 2D Materials and Applications* **7**, 32 (2023).
- [42] C. Fournier, A. Plaud, S. Roux, A. Pierret, M. Rosticher, K. Watanabe, T. Taniguchi, S. Buil, X. Quélin, J. Barjon, *et al.*, *Nature communications* **12**, 3779 (2021).
- [43] E. J. Lenferink, T. LaMountain, T. K. Stanev, E. Garvey, K. Watanabe, T. Taniguchi, and N. P. Stern, *ACS Photonics* **9**, 3067 (2022).
- [44] M. M. Ugeda, A. J. Bradley, S.-F. Shi, F. H. Da Jornada, Y. Zhang, D. Y. Qiu, W. Ruan, S.-K. Mo, Z. Hussain, Z.-X. Shen, *et al.*, *Nature materials* **13**, 1091 (2014).
- [45] A. Raja, A. Chaves, J. Yu, G. Arefe, H. M. Hill, A. F. Rigosi, T. C. Berkelbach, P. Nagler, C. Schüller, T. Korn, *et al.*, *Nature communications* **8**, 15251 (2017).
- [46] A. Steinhoff, M. Florian, M. Rösner, G. Schönhoff, T. O. Wehling, and F. Jahnke, *Nature communications* **8**, 1166 (2017).
- [47] C. Forsythe, X. Zhou, K. Watanabe, T. Taniguchi, A. Pasupathy, P. Moon, M. Koshino, P. Kim, and C. R. Dean, *Nature nanotechnology* **13**, 566 (2018).
- [48] C. C. Price, N. C. Frey, D. Jariwala, and V. B. Shenoy, *ACS nano* **13**, 8303 (2019).
- [49] P. Moser, L. M. Wolz, A. Henning, A. Thurn, M. Kuhl, P. Ji, P. Soubelet, M. Schalk, J. Eichhorn, I. D. Sharp, *et al.*, *Advanced Functional Materials* , 2418528 (2024).
- [50] M. Heithoff, Á. Moreno, I. Torre, M. S. Feuer, C. M. Pursler, G. M. Andolina, G. Calajò, K. Watanabe, T. Taniguchi, D. M. Kara, *et al.*, *ACS nano* **18**, 30283 (2024).
- [51] J. Hu, E. Lorchat, X. Chen, K. Watanabe, T. Taniguchi, T. F. Heinz, P. A. Murthy, and T. Chervy, *Science Advances* **10**, eadk6369 (2024).
- [52] L. Cavalcante, D. R. da Costa, G. Farias, D. Reichman, and A. Chaves, *Physical Review B* **98**, 245309 (2018).
- [53] D. K. Efimkin and A. H. MacDonald, *Physical Review B* **95**, 035417 (2017).
- [54] A. Guarino, G. Poberaj, D. Rezzonico, R. Degl’Innocenti, and P. Günter, *Nature photonics* **1**, 407 (2007).
- [55] C. Wang, M. Zhang, X. Chen, M. Bertrand, A. Shams-Ansari, S. Chandrasekhar, P. Winzer, and M. Lončar, *Nature* **562**, 101 (2018).
- [56] M. He, M. Xu, Y. Ren, J. Jian, Z. Ruan, Y. Xu, S. Gao, S. Sun, X. Wen, L. Zhou, *et al.*, *Nature photonics* **13**, 359 (2019).
- [57] M. Zhang, C. Wang, R. Cheng, A. Shams-Ansari, and M. Lončar, *Optica* **4**, 1536 (2017).
- [58] B. Wen, Y. Zhu, D. Yudistira, A. Boes, L. Zhang, T. Yidirim, B. Liu, H. Yan, X. Sun, Y. Zhou, *et al.*, *ACS nano* **13**, 5335 (2019).
- [59] C. H. Li, K. M. McCreary, and B. T. Jonker, *ACS omega* **1**, 1075 (2016).
- [60] D. Li, X. Huang, Z. Xiao, H. Chen, L. Zhang, Y. Hao, J. Song, D.-F. Shao, E. Y. Tsybal, Y. Lu, *et al.*, *Nature communications* **11**, 1422 (2020).
- [61] K. Gallo, C. Gawith, and P. Smith, *Ferroelectrics* **340**, 69 (2006).
- [62] S. Cherifi-Hertel, H. Bulou, R. Hertel, G. Taupier, K. D. Dorkenoo, C. Andreas, J. Guyonnet, I. Gaponenko, K. Gallo, and P. Paruch, *Nature communications* **8**, 15768 (2017).
- [63] T. Jungk, Á. Hoffmann, and E. Soergel, *Physical Review B* **89**, 226101 (2014).
- [64] A. N. Morozovska, E. A. Eliseev, G. S. Svechnikov, V. Gopalan, and S. V. Kalinin, *Journal of Applied Physics* **103** (2008).
- [65] P. Soubelet, J. Klein, J. Wierzbowski, R. Silvioli, F. Sigger, A. V. Stier, K. Gallo, and J. J. Finley, *Nano Letters* **21**, 959 (2021).
- [66] A. Castellanos-Gomez, M. Buscema, R. Molenaar, V. Singh, L. Janssen, H. S. Van Der Zant, and G. A. Steele, *2D Materials* **1**, 011002 (2014).
- [67] J. Liu, W. Chen, B. Wang, and Y. Zheng, *Materials* **7**, 6502 (2014).
- [68] J. S. Ross, S. Wu, H. Yu, N. J. Ghimire, A. M. Jones, G. Aivazian, J. Yan, D. G. Mandrus, D. Xiao, W. Yao, *et al.*, *Nature communications* **4**, 1474 (2013).
- [69] A. O. Slobodeniuk and M. R. Molas, *Physical Review B* **108**, 035427 (2023).
- [70] C. Chakraborty, K. M. Goodfellow, and A. Nick Vamivakas, *Optical Materials Express* **6**, 2081 (2016).
- [71] T. Cao, G. Wang, W. Han, H. Ye, C. Zhu, J. Shi, Q. Niu, P. Tan, E. Wang, B. Liu, *et al.*, *Nature communications* **3**, 887 (2012).
- [72] K. F. Mak, K. He, J. Shan, and T. F. Heinz, *Nature nanotechnology* **7**, 494 (2012).
- [73] Q. Wang, J. Maisch, F. Tang, D. Zhao, S. Yang, R. Joos, S. L. Portalupi, P. Michler, and J. H. Smet, *Nano letters* **21**, 7175 (2021).
- [74] M. M. Glazov, E. L. Ivchenko, G. Wang, T. Amand, X. Marie, B. Urbaszek, and B. Liu, *physica status solidi (b)* **252**, 2349 (2015).
- [75] J. Jadczyk, J. Kutrowska-Girzycka, P. Kapuściński, Y. Huang, A. Wójs, and L. Bryja, *Nanotechnology* **28**, 395702 (2017).
- [76] L. Li, H. Yang, and P. Yang, *Journal of Colloid and Interface Science* **650**, 1312 (2023).
- [77] M. J. Missey, S. Russell, V. Dominic, R. G. Batchko, and K. L. Schepler, *Optics Express* **6**, 186 (2000).